

3D Printing Functionally Graded Porous Materials for Simultaneous Fabrication of Dense and Porous Structures in Membrane-Integrated Fluidic Devices

Hari Kalathil Balakrishnan, Ludovic F. Dumée, Andrea Merenda, Cyril Aubry, Dan Yuan, Egan H. Doeven,* and Rosanne M. Guijt*

3D printing provides access to complex multilevel architectures, though the capability to routinely print and integrate structures of controlled porosity is limited. Herein, grayscale digital light projection 3D printing of a polymerization-induced phase separation ink is introduced to directly 3D print functionally graded porous within a single layer from the same ink formulation. The structural properties of materials printed from a single ink are tuned from an effectively dense to a porous material with interconnected pores up to 250 nm.

Heterostructures with the physically dense structure of porosity 0.8% and porous structures with up to 23% can be concurrently formed within a layer, with high spatial resolution inherent of this 3D printing technique. Materials with densities from 1.01 to 1.21 g cm⁻³ are 3D printed in a wicking device and show wicking rates (H₂O) from complete diffusion blockage up to 4.5 mm h⁻¹. Furthermore, a proof-of-concept membrane-integrated fluidic device is used for the elemental metal sensing of iron in soil. The presented single-step fabrication of functionally graded materials with pixel-based control within a single layer holds potential for manufacturing and integrating membranes or sorbents for environmental, biotechnology, and healthcare applications.

1. Introduction


The combination of microfluidics and material science has led to a breakthrough in ordered porous materials.^[1] Single-phase porous materials with a large surface area confined within small volumes facilitate physical exclusion or selective adsorption of unwanted contaminants or chemical species. However, several necessary fields of applications, such as energy storage, fluid filtration, and especially in tissue engineering, require spatially varying porosity or pore size with well-defined gradients.^[2,3] Porous materials can be created synthetically or microfabricated using lithographic and/or advanced additive/subtractive approaches, providing various degrees of control over the morphological and chemical properties.^[4,5]

3D printing, also referred to as additive manufacturing (AM), offers unprecedented opportunities to design and produce complex architectures. Moreover, custom-designed geometries can be fabricated rapidly and cost effectively, including layouts

H. K. Balakrishnan, D. Yuan, E. H. Doeven, R. M. Guijt
Centre for Rural and Regional Futures
Deakin University
Locked Bag 20000, Geelong, VIC 3320, Australia
E-mail: egan.doeven@deakin.edu.au; rosanne.guijt@deakin.edu.au

H. K. Balakrishnan, A. Merenda
Institute for Frontier Materials
Deakin University
Locked Bag 20000, Geelong, VIC 3320, Australia

L. F. Dumée
Department of Chemical Engineering
Khalifa University
Abu Dhabi, United Arab Emirates

 The ORCID identification number(s) for the author(s) of this article can be found under <https://doi.org/10.1002/ssstr.202200314>.

© 2023 The Authors. Small Structures published by Wiley-VCH GmbH. This is an open access article under the terms of the Creative Commons Attribution License, which permits use, distribution and reproduction in any medium, provided the original work is properly cited.

DOI: 10.1002/ssstr.202200314

L. F. Dumée
Research and Innovation Centre on CO₂ and Hydrogen
Khalifa University
Abu Dhabi, United Arab Emirates

L. F. Dumée
Centre for Membrane and Advanced Water Technology
Khalifa University
Abu Dhabi, United Arab Emirates

A. Merenda
School of Science
RMIT University
124 La Trobe Street, Melbourne, VIC, Australia

C. Aubry
Research Laboratories
Khalifa University
Abu Dhabi, United Arab Emirates

E. H. Doeven
School of Life and Environmental Sciences
Deakin University
Locked Bag 20000, Geelong, VIC 3320, Australia

that cannot be manufactured with classical machining, molding, or lithographic techniques.^[6] Incorporating materials with special morphologies and architectures like porosity^[7] within 3D-printed objects is an innovative approach and emerging area of research, combining the benefits of 3D printing with the functionalities offered by porous materials.^[8] Previous efforts to combine porous and dense materials using fused filament fabrication (FFF) using multiprint head printers have been demonstrated.^[8–11] However, the porous properties offered by commercial filament materials are not adjustable and defined by the original filament composition.^[12,13] Similarly, the integration of porous and dense materials has been demonstrated using artifacts of the printing process in polyinkjet printing (PIP), an approach that does not provide control of the porous properties.^[9] Early steps toward printing porous materials were demonstrated by inks containing inert templates,^[12] which were removed to reveal the material's porous nature.^[14,15] Alternatively, modified/integrated 3D printers based on extrusion techniques using bioinks were used for developing homogeneous porous structures by stacking bioinks in different levels.^[16]

Polymerization-induced phase separation (PIPS) is an alternative approach for synthesizing porous materials in a controllable manner.^[17] The polymerization process induces the formation of polymer-rich and polymer-poor phases, with the latter providing a template for the pores when the polymer-rich phase solidifies.^[18] PIPS inks in AM provide an attractive opportunity to 3D print porous objects directly. Porous polymers were formed from a PIPS ink using a two-photon polymerization (TPP) process, revealing that the exposure time can be used to tune the porosity and porous properties of the final materials.^[19] Digital light projection (DLP), a faster and more accessible technique than TPP that relies on photopolymerization, was used to directly generate porous glass structures by introducing phase separation in a purpose-developed photopolymerizable ink.^[20] A similar principle was also used to print nanoporous polymeric objects up to a few centimeters, where control over the porosity and pore size distribution was obtained by altering the ink's composition.^[21] These resin exchange strategies and the exposure time modulation could be adapted for developing graded porous materials. However, since only a single-phase structure is generated at a time within a layer and/or a plane, the variation is only possible in a single plane. Unfortunately, this limits the combination of elements with varying porosity within a layer (that provides the modulation in XY and Z plane), which is required for specialized applications and functional integration. Moreover, this binary approach to material integration is in stark contrast with most materials found in nature, where materials are functionally graded to provide improved characteristics.^[22,23] The capacity to manufacture functionally graded materials (FGM) is sought to enhance the material performance characteristics. Along these lines, a process involving grayscale DLP (G-DLP) demonstrated the proof of concept for printing FGM with tunable mechanical properties.^[24] The variation in mechanical properties is linked to modulation of the thermal postcuring stage.

The innovation in the present work is the modulation of the irradiation dose using G-DLP to control the porosity of materials formed from photopolymerizable inks undergoing phase separation upon polymerization, facilitating the formation of

functionally graded porous materials. Importantly, the pixel-level control of grayscale provides control of the spatial distribution of the porous domains within a single layer, providing control of the material porosity in *x*, *y*, and *z* directions of the fabricated part, and does not require additional postprocessing steps. The potential of integrating these materials is illustrated by fabricating functionally integrated fluidic devices combining dense and porous areas concurrently printed in a single fabrication step. This device was used for colorimetric iron determination in soil samples. Future applications of this new approach are anticipated to expand from functionally integrated devices for particle separation, to integrated 3D printed devices for chromatography, and FGM for scaffolding in cell and tissue culture and other biologically inspired materials.^[2,25]

2. Theory and Calculations

2.1. Light Dose

In DLP, the crosslinking (polymerization) of the resin depends on the light dose *D* received for every layer, which in turn is determined by the light intensity *I* and the layer exposure time *t_l*. For each ink and printer combination, the critical light dose, *D_c*, is the dose at which ink polymerization has proceeded far enough to result in a solid or nearly solid material in a single layer. For a layer height *z_p*, *D_c* is expressed as a function of the exposure time, *t_l*, the light intensity at the bottom of the vat *I₀*, and *h_a*, the penetration depth dictated by the optical properties of the resin.^[26]

$$D_c = t_l I_0 e^{-\frac{z_p}{h_a}} \quad (1)$$

where *I₀* and *h_a* are constant for a given printer and ink formulation. The printing depends on the light intensity *I* and the layer exposure time *t_l*. Since the manipulation of exposure time could only provide modulation of properties in one plane, it is necessary to control the intensity within the individual irradiated layer to modulate properties in the *X*, *Y*, and *Z* planes.

Conventionally, the exposure across the layer is binary since individual pixels are turned on or off to achieve the projected image. In G-DLP, however, the intensity *I* is modulated at the individual pixel level using a grayscale mask, decreasing the intensity at the individual pixel, *I_p*, from the intensity of the layer *I_l* by the percentage grayscale *GS (P)*.

$$I_p = \left(1 - \frac{GS(P)}{GS(100)}\right) \times I_l \quad (2)$$

GS (P) ranges from *GS (0)*, where no grayscale mask is imposed (*I_p* = *I_l*), and *GS (100)* is the maximum grayscale intensity (100%). Grayscale masks are used to improve the homogeneity of the light intensity across the build space or for antialiasing. However, this feature can provide different grayscale intensities for different pixels across a single layer, hence providing different light intensities within various areas of a single layer. This modulation of the energy dose at the pixel level is proposed here to control the porosity of PIPS.

For this work, it is also essential to realize that D_c is the minimum dose required to form a porous structure, and D needs to be increased to create a dense material.

2.2. PIPS Ink Formulation

For the formation of porous polymeric materials by phase separation,^[27] a porogen needs to be included in the ink to precipitate the forming polymer. Formulations for porous polymer monoliths made by PIPS typically combine a good and a bad porogen with high and low solubility of the polymer to facilitate macro- and micropore formation. Here, PEGDA-250 was selected as a monomer for its fast polymerization kinetics, as previously demonstrated to be advantageous in DLP for printing highly accurate closed microfluidic voids,^[13] as well as for the preparation of polymer monoliths by PIPS.^[28] Furthermore, methanol was used as a single porogen in the PIPS ink, a simplification afforded by the envisioned application in soil testing that solely relies on microporous properties to transport aqueous solutions and, unlike chromatographic applications, is not reliant on the high surface area.

In PIPS, the porous properties are determined by the irradiation intensity, duration and wavelength, the temperature, and the composition of the ink, which contains initiators, monomers, and porogen. In the early stage of the polymer formation, the formed oligomers remain dissolved in the ink and, as the polymerization process continues, merge into polymeric mesodomains that are no longer soluble. This decrease in solubility due to the shift in surface energy arising from the polymerization process and the elimination of functional groups leads to the phase separation and precipitation process, supporting the formation of the permanent porous domains/globules. The polymer network will extend using these nuclei as a seed while the formation of new oligomers also continues in solution, forming new nuclei. The porogen in ink formulation plays an important role as its chemistry influences the phase separation and its concentration the void volume. When the porogen has a high affinity toward nuclei, oligomer formation will be inhibited, resulting in smaller globules. On the contrary, if the porogenic solvent has a low affinity for the oligomers, phase separation occurs earlier and larger globular structures are formed.^[29] In addition, the porogenic solvents prevent the collapse of the pores by filling the voids, ensuring structural integrity through consistent distribution across the material.^[18] The porogen can be removed after the crosslinking as it does not participate in the polymerization.

The porogen content of the PIPS ink used in this work was optimized for printing porous and dense materials at high- and low-exposure doses to enable their formation in a single print. The permeability of the materials formed was assessed experimentally by observing a droplet of water deposited on the material surface, where a permeable material was defined as a material where the water readily was absorbed into the material and nonpermeable (dense) material as a material where the water remained on the surface for >1 min. For an ink formulation containing 42% ($v V^{-1}$) porogen, a no-permeable material was formed for an exposure time of 156 s, five times D_c (for this ink, $t_1 = 30$ s). Materials printed from inks with a porogen content >42% facilitated the diffusion of water into the material

even when exposed to higher D . Aiming for material with maximal permeability, the maximum porogen content that still allowed for the formation of an impermeable material at an exposure of $5t_1$ (five times normal layer exposure) was selected at 42% ($v V^{-1}$) methanol and used to investigate the effect of grayscale masks on the materials' porous properties.

3. Results and Discussion

3.1. Grayscale DLP 3D Printing of Functionally Graded Porous Materials

During DLP, the ink is exposed to UV light in a layer-by-layer manner using the LCD screen, providing a faster printing process than stereolithography (SLA), where a point-by-point exposure process using a laser light source is used. DLP printers like the Phrozen Shuffle used here can be obtained for US\$400 and provide a rapid and seamless translation of digital information developed using CAD software to a complex 3D physical object ($120 \times 70 \text{ cm}^2$ with a vertical printing speed of 3 cm h^{-1}). The optical engine of the Phrozen Shuffle printer used in this work, the Para LED-based array matrix, generates consistent illumination across the LCD, enabling fast and uniform curing along with the layer. Akin to other 3D printing techniques, the designed structures were sliced into individual images representing single-curing layers (Figure S1b, Supporting Information). In G-DLP, a grayscale mask can be associated with the sliced images for sequential projection at attenuated intensity, controlled at a pixel-by-pixel level (Figure 1a).

As discussed in Section 3.2, the ink formulation was optimized to yield a nonpermeable material when exposed at $5t_1$ using a full exposure/bright screen at zero light attenuation using a grayscale intensity of 0% (GS-0). As illustrated in Figure 1a, grayscale mask intensities between 0% (GS-0, $I_p = I_1$) and 100% (GS-100, $I_p = 0$) were used to print test objects, resulting in the printing of complete structures between GS-0 and GS-75, but incomplete structures at grayscale intensities >GS-75 because $D < D_c$. This upper limit is comparable with the GS-85 limit reported for an ink developed for creating FGM using a multistage crosslinking process involving photo- and thermally initiated polymerization.^[24]

3.2. Material Characterization

We hypothesize that with increasing grayscale intensity, crosslinking decreases, decreasing the density of the porous network while increasing its porosity, as illustrated in Figure 1b. Using the optimized ink formulation (42% ($v V^{-1}$) methanol, Section 3.2), a nonpermeable material was formed using $D = 5D_c$. Materials printed at $D = 5D_c$ using GS-0, GS-45, GS-55, GS-65, and GS-75 were visualized by high-resolution SEMs (Figure 2a), confirming the expected trend toward a more open morphology with increasing grayscale intensity. A dense polymer structure was obtained for the full-light irradiance at no grayscale condition (GS-0), confirming the impact of the modulated irradiation on the phase separation and pore formation process. This agrees with the material's inability to absorb water in the droplet test. A noticeable difference in polymer volume was

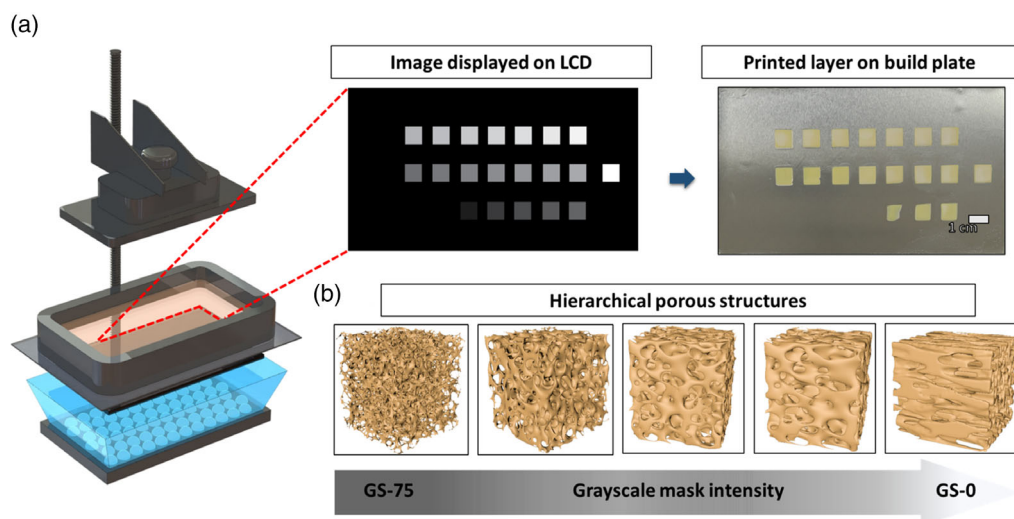


Figure 1. Grayscale DLP concept: a) In grayscale DLP 3D printing, an image combined with the grayscale mask with intensities varying from GS-0 to GS-100 (interval $\sim 5\%$) is displayed on the LCD screen. Polymerization is induced in the hybrid ink during UV exposure to form a single layer (thickness = $100\ \mu\text{m}$). A controlled exposure greater than GS-75 results in partial and/or incomplete layer formation. (b) Graphical representation of the impact of G-DLP combined with PIPS: controlled exposures between GS-0 and GS-75 in the hybrid ink result in the formation of hierarchically porous structures.

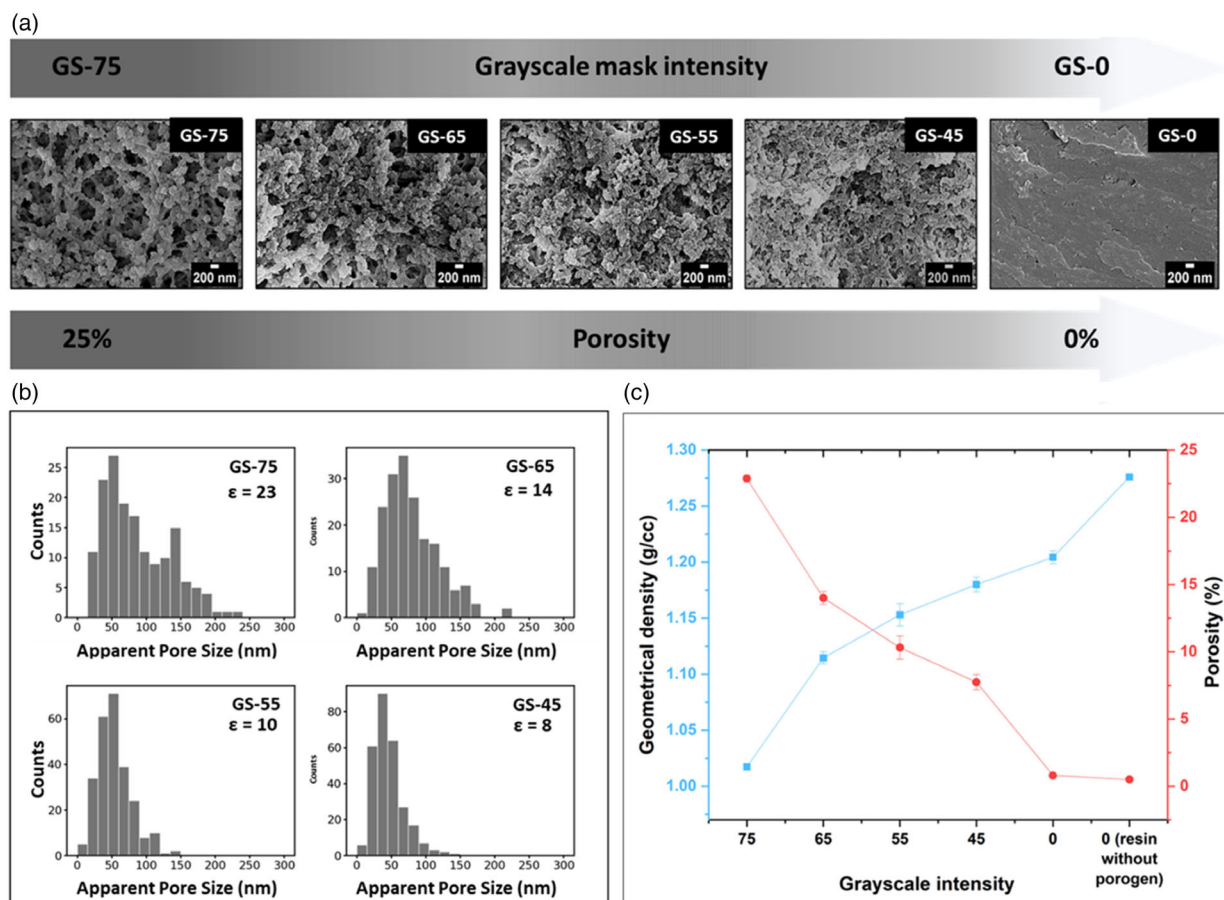


Figure 2. Structural evaluation: a) SEM images along the cross-sectional plane of square blocks printed under grayscale intensities (GS-0, GS-45, GS-55, GS-65, GS-75) demonstrate the porous morphology gradient. b) Pore size analysis: pore size was calculated from the analysis for all the grayscales. c) Variation of porosity and geometrical density for different grayscale exposure conditions.

revealed for the GS-75 samples, showing globular polymeric structures in the sub- μm region ($<500\text{ nm}$), typically a characteristic of PIPS materials, while lower grayscales showed increasingly dense structures.

To quantify the differences between the materials printed at different GS, the pore size was calculated from the SEM images based on the Euclidean distance transform method (Figure S2, Supporting Information)^[19] (Figure 2b). A broad size distribution of pores between 0 and 250 nm, with a maximum pore size between 200 and 250 nm, was found for the given formulation printed under GS-75. Although the maximum pore size for material printed with GS-65 was close to 150 nm, accompanied by a narrower pore size distribution (60–150 nm), the material printed with GS-55 had no pores greater than 150 nm and a narrower distribution between 50 and 100 nm. Using GS-45, a material with a higher pore count between 0 and 50 nm was obtained with a pore size distribution between 0 and 100 nm. This analysis confirms that the pore size gradually decreases, and a tighter pore size distribution is obtained as the grayscale intensity decreases (Figure 2b).

The volumetric features of the materials printed using GS-0, GS-45, GS-55, GS-65, and GS-75 were analyzed based on the geometrical and skeletal densities (Figure 2c). A significant difference in the geometrical density was identified for GS-75 (1.01 g cm^{-3}) compared to GS-0 (1.21 g cm^{-3}). The geometrical density increased gradually with decreasing grayscale intensity, from 1.11 g cm^{-3} for GS-65 to 1.15 g cm^{-3} for GS-55 and 1.18 g cm^{-3} for GS-5. The geometrical density obtained at GS-0 was lower than the density of the sample prepared using an ink formulation without porogen (1.28 g cm^{-3}). This can be explained by the presence of the porogen in the ink (42% (v/v) methanol), which does not participate in polymerization. The porosity was derived from the skeletal density measured using an ultrapycnometer and ranged from 23% for GS-75

to 0.8% for GS-0 (Figure 2c). A gradual decrease in porosity was found with increasing grayscale intensity. The porosity for the nonporogen-containing ink formulation was 0.5%, similar to that of the material obtained with GS-0.

Most AM approaches rely on adhesion between sequentially deposited layers, except for volumetric 3D printing. SEM imaging was used to study the layer interface in the GS-0 and GS-75 materials (Figure 3). Images of both five printed layers (left) and a close-up of the interface between the layers (right) are provided in Figure 3. The absence of voids and cracks at the layer interface indicates excellent layer-to-layer adhesion for both conditions at the layer interface in both materials. Furthermore, the “ghost prints” generated by the individual pixels ($47 \times 47\text{ }\mu\text{m}^2$) from the LCD can also be observed, a common feature in DLP. The layered structural morphology and the interface bonding are identical to the other grayscales studied and provided in Figure S3, Supporting Information.

In addition to cross-sectional and bulk morphology, for a better understanding of the surface morphology, a 3D laser microscope was used to record the surface morphology and surface roughness (Figure S4, Supporting Information). The surface images and the surface profile clearly showed the pixel impressions replicated from the LCD screen. The surface roughness linearly increased with an increase in the grayscale mask intensity, where the minimum surface roughness (S_q) was identified for GS-0 ($.959\text{ }\mu\text{m}$) and maximum for GS-75 ($1.489\text{ }\mu\text{m}$) (Figure S5, Supporting Information).

Porosity is the result of the presence of the porogen in the ink, which does not participate in polymerization. During G-DLP, the light intensity is modulated, leading to a modulation in polymerization kinetics/rate, and results in the formation of different skeletal structure.^[30] Chemical similarity was confirmed by ATR spectroscopy, as presented in Section S4, Supporting Information. The spectra confirm the absence of methanol

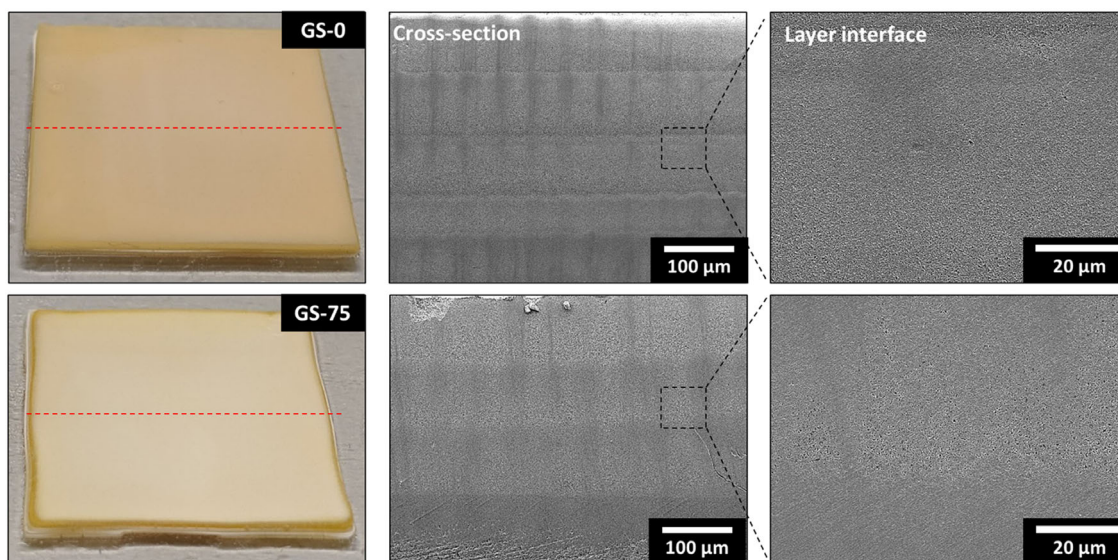


Figure 3. Layer interface adhesion: square block ($4 \times 4 \times 0.5\text{ mm}$) printed under GS-0 condition and GS-75 condition (left). SEM image of entire print layers recorded along the cross section of the GS-0 region (center). Image recorded at the interface between two layers (GS-0) (right). SEM image of entire print layers recorded along the cross section of the GS-75 region (center). Image recorded at the interface between two layers (GS-75) (right).

and hence demonstrate effective removal of the porogen. Additionally, the loss of the $=CH_2$, alkene of acrylate group found in the monomer from the printed material, confirms the absence of free monomer in the materials formed under GS-0 and GS-75 conditions (Figure S7, Supporting information). Tuning of the polymerization kinetics and rate is used to optimize the porosity and permeability of polymer monoliths used as stationary phases used in chromatography. The more porous materials are not simply underpolymerized; instead, they reflect the differences in the polymerization process in the formation of and growth from the backbone. It should be noted the monomer conversion in polymer monoliths is typically $<100\%$ and unpolymerized monomer is washed out with the porogen.^[30] Here, a merely dense network is formed under full exposure conditions, with the chemical composition dictated by the monomer (PEGDA).

The postprocessing involved the removal of the porogen by washing the material with isopropanol, followed by air drying. The materials developed with various grayscale intensities exhibited different shrinkage rates in X, Y, and Z directions. Shrinkage in all directions increased as the grayscale intensity increased. Shrinkage rate in the XY plane was comparable; however, the shrinkage rate in the Z direction was larger for the GS-75 (7.33%) than for GS-0 (4.23%). Though the layers are printed in $100\ \mu\text{m}$ layers, the higher shrinkage during postprocessing of areas printed at higher grayscale intensities leads to lower structures than those that were fully exposed. This resulted in a less evident staircase effect for the grayscale cured structures. Shrinkage of PIPS materials is well known and can lead to cracking,^[31] while shrinkage can be reduced by decreasing the porogen content; this will impact the porous properties. Materials printed from nonporogen-containing inks exhibited 0.09% volumetric shrinkage, whereas shrinkage rates of 10.51% and 14.20% were observed following porogen removal for the GS-0 and GS-75 inks, respectively (Table S1, Supporting Information).

3.3. Functionally Graded Porous Material-Integrated Fluidic Devices

3.3.1. Wicking Device

The extent of control of the structural and volumetric features of the materials printed by G-DLP was evaluated with a device designed and printed with discrete regions with grayscale intensities ranging from GS-45 to GS-75 (Figure 4a (top and bottom)). The wicking behaviors of the materials produced at different grayscale intensities were studied using GS-0 as a reference, excluding materials with grayscale intensity below 45% because of poor wicking rates ($0.5\ \text{mm h}^{-1}$). The test device included reservoirs with a volume of $20\ \mu\text{L}$ defined by a nonpermeable boundary printed at GS-0, interrupted to provide fluidic access to materials printed using GS-75, GS-65, GS-55, GS-45, and GS-0. Test devices containing these five strips were printed in a single print from single ink formulation. The wicking front of the aqueous solutions containing fluorescein for visualization was monitored over 8 h in the rectangular strips with a cross-sectional area of $4 \times 0.5\ \text{mm}^2$, with the differences in the progression of the liquid front shown in Figure 4b (top and bottom)). The progression of the liquid through the material increased with increasing grayscale intensity, recording the fastest wicking rate in GS-75. No wicking was observed in GS-0, confirming that a dense material was formed. The time-resolved data confirm the faster progression of the liquid front for the increased grayscale intensity (Figure 4c) and show that the wicking rate slows down over time. The wicking rate results from a delicate balance of pores small enough to create sufficient capillary pressure but large enough to provide high permeability to minimize resistance. In polymer monoliths, a higher transport rate typically corresponds with a larger pore diameter;^[32] hence, the wicking rates agrees with the pore size measurements presented in Figure 2b, where the largest pores up to $250\ \text{nm}$ were found for the GS-75 samples. The analysis of the wicking kinetics provided

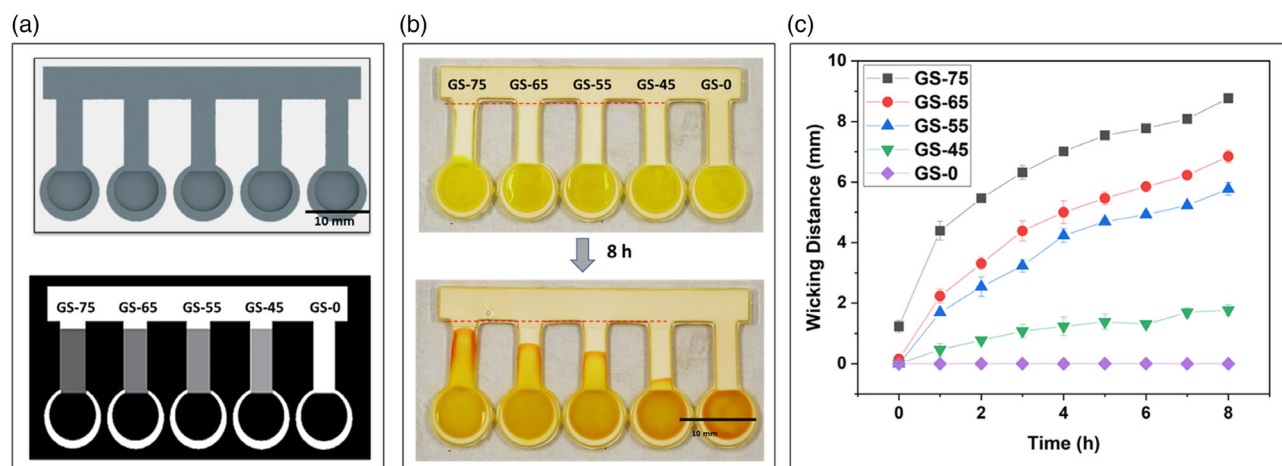


Figure 4. Wicking experiment: a) Design: The device comprises circular reservoirs of $20\ \mu\text{L}$ volume connected to rectangular strips with $4 \times 0.5\ \text{mm}$ cross sections and $9\ \text{mm}$ length (top) and a single layer displayed on the LCD screen with a grayscale mask (bottom). Exposure of the rectangular strips is controlled using grayscale masks of intensities GS-75, GS-65, GS-55, and GS-45 and the full exposure region of GS-0. b): Printed device using G-DLP demonstrating wicking behavior. c) Wicking distance of fluorescein solution at time points through the rectangular strips with different grayscale masks.

further insight into the porosity and volumetric structural details. Darcy's law relates the flow velocity and the pressure fields;^[33] the flow rate is proportional to the pressure drop and inversely propositional to the pore distribution. The highest wicking rate in the first hour (4.5 mm h^{-1}) was obtained for GS-75, the material with the largest pore size and range (0–250 nm). Then, the wicking rate slowly decreased to 2.2 mm h^{-1} (GS-65, pore distribution 60–150 nm) and 1.7 mm h^{-1} (GS-55, pore size distribution 50–100 nm), followed by a substantial decrease in the wicking rate for GS-45 (0.5 mm h^{-1}), suggesting its small pores (<100 nm) and low porosity limit

3.4. Porous and Dense Material for Membrane-Integrated Fluidic Devices

Porous materials can form a size-selective barrier and provide a large surface area for chromatographic, catalytic, and energy storage materials or a scaffold for cell culture. Therefore, 3D printing of functionally graded porous structures has the potential to enable a leap in the fabrication of functionally integrated fluidic

devices.^[8] Here, G-DLP using a PIPS ink was used to print a functionally integrated fluidic device for soil analysis.^[34] In order to demonstrate the potential of the technique, a fluidic device consisting of two chambers separated by a porous 3D printed membrane was designed using grayscale masks of GS-0 and GS-75 for the dense and porous areas, respectively (Figure 5a). The dense material retains the sample and reagents within the chambers, and the porous membrane enables the transport of solutes while limiting the transport of particulate matter.

When a formulation developed for polymer monoliths was used directly in G-DLP, uncontrolled polymerization at the edges compromises the accuracy of the translation of the model into a 3D-printed object, particularly for the high dose delivered for printing dense material (Figure 5b (left)). The material in these regions, recognizable by the more intense white appearance than the other areas (material volume = 70.7 mm^3), is anticipated to display a gradient in porosity due to changing polymerization characteristics away from the originally exposed areas, thus leading to the wicking of the reagents along the edges of the

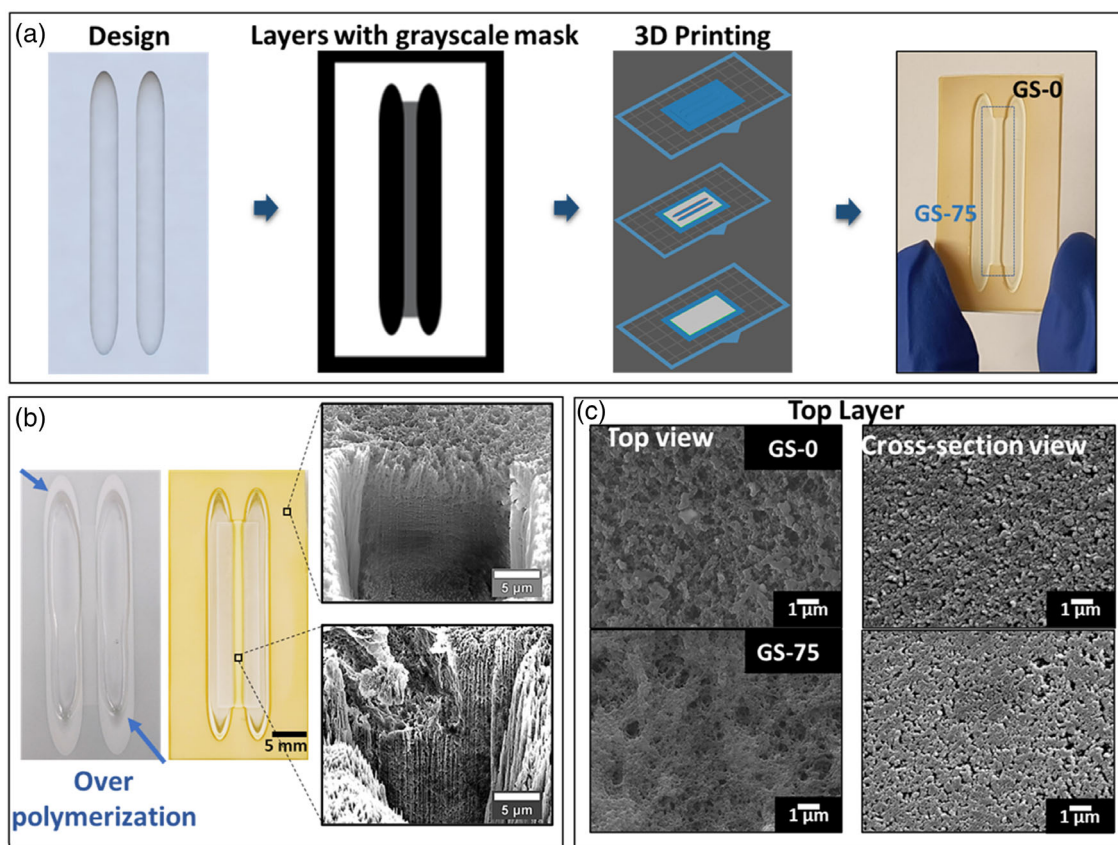


Figure 5. Membrane-integrated fluidic device: a): The fluidic device was designed with two reservoirs ($30 \times 3 \text{ mm}$) parted with a separation barrier (2 mm) through grayscale DLP 3D printing combined with PIPS. The projected image of the design on the LCD screen with exposure of the separation barrier region was controlled by GS-75, while for the remainder of the projected image, GS-0 was used. 3D-printed device (overall dimensions: $36 \times 18 \times 0.5 \text{ mm}$) b): In a device developed by the conventional bulk polymerization-based resin formulation (left), uncontrolled polymerization along the edges of the reservoir and at the porous barrier region is denoted. The device was developed using the hybrid ink formulation to limit the overpolymerization and fine control the porous structure. (right) FIB-SEM images revealing the surface porosity transition effect c): SEM image from the top view for GS-0 condition, showing porous morphology. SEM image recorded from the top layer/edge cross section for the GS-0 condition. SEM image recorded from the top view for GS-75 condition, showing porous morphology. SEM image recorded from the cross section of the top layer/edge for the GS-75 condition.

reservoirs. Furthermore, the porous membrane separating the reservoirs was significantly wider than designed (65.5% by volume), indicating poor replication of the designed features. Photoabsorbers have previously been used to limit the formation and quench radicals to halt the polymerization reaction and maintain the spatial resolution in the z-direction.^[26] Here, incorporating a photoabsorber improved the dimensional accuracy in the xy plane and enabled the localized control of the porous and dense properties (Figure 5b (center)). For the photoabsorber containing ink, h_a was minimized using $0.015\% \text{ w W}^{-1}$ of photoabsorber for the ink containing $42\% \text{ v V}^{-1}$ porogen, based on previously developed procedures.^[13,26] The photoabsorber was included in the inks used for material characterization to ensure consistency throughout this work.

The structural properties of GS-0 and GS-75 were further investigated by recording the FIB–SEM and SEM cross sections close to the top surface/layer, as shown in Figure 5b (right). Although a dense morphology was expected in the GS-0 region, a porous structure similar to GS-75 was observed close to the top edge. The observed porous top surface is thought to be an artifact of the DLP 3D printing process caused by the Teflon film at the bottom of the resin tank since the oxygen permeability of fluorinated polymers was previously demonstrated to generate dead zones to prevent the adhesion of the printed layer to the vat tank.^[21,35] Akin to the lower light intensity, this inhibition of the polymerization reaction will yield a more porous material. SEM–FIB imaging revealed that the transition from porous to dense structures occurred ten μm from the top of the layer for GS-0. Farther away from the top edge, the material progressively transcended to a dense, polymer-filling phase. In contrast, uniform and highly porous structures were maintained moving down from the surface for materials made using GS-75 (Figure 5b (right)). Furthermore, SEM images were recorded close to the top edge of the topmost layer to confirm the analysis from SEM–FIB images (Figure 5c). The top view of the top layers for both GS-0 and GS-75 samples represents a highly porous structure (Figure 5c (left)). However, in the cross-section SEM

images, the GS-75 sample represents a morphology with pores throughout, while the GS-0 sample developed a rough but dense structure without visible pores (Figure 5c (right)).

3.4.1. Porous and Dense Material Interface

G-DLP 3D printing of PIPS ink enables the development of functionally graded porous materials by controlling the porosity in the X–Y plane (within a layer) and the Z plane, while the alternative strategies, such as changing the porogen concentrations or exposure time, only yield the change in porosity in the Z plane (over multiple layers). Thus G-DLP provides modulation of porosity in a single layer, which opens the potential for simultaneous fabrication of porous and dense structures. This is a critical requirement in the one-step fabrication of membrane-integrated fluidic devices. A transition zone from porous to the dense structure is developed at the interface between GS-75 and GS-0. The surface morphology was analyzed using the optical profilometer, and SEM images were recorded for cross-sectional structure evaluation. Surface images clearly showed a transition zone at the interface equivalent to 3–4 pixels (1 pixel = $47 \mu\text{m}$) (Figure 6a). Furthermore, a 6–7 μm difference in the surface profile between GS-0 and GS-75 was observed. This difference accounts for the shrinkage rate variation between GS-75 (7.33%) and GS-0 (4.23%) in the Z direction upon drying (Table S1, Supporting Information). The increase in thickness about $15 \mu\text{m}$ at the gray mask interface is even more interesting. We believe that at the interface, the monomer not consumed under GS-75 conditions is incorporated in the GS-0 material, creating a more crosslinked, denser material with less shrinkage than GS-0. A similar effect has been reported elsewhere as increased bulging effects with layer height and the channel sides.^[13]

SEM images recorded along the interface also showed the porosity variation between the two zones. The transition zone $< 200 \mu\text{m}$ aligns with the surface transition zone observations (Figure 6b (left)). This transition zone over the 3–4 pixels is probably due to the light scattering effect and the extension of

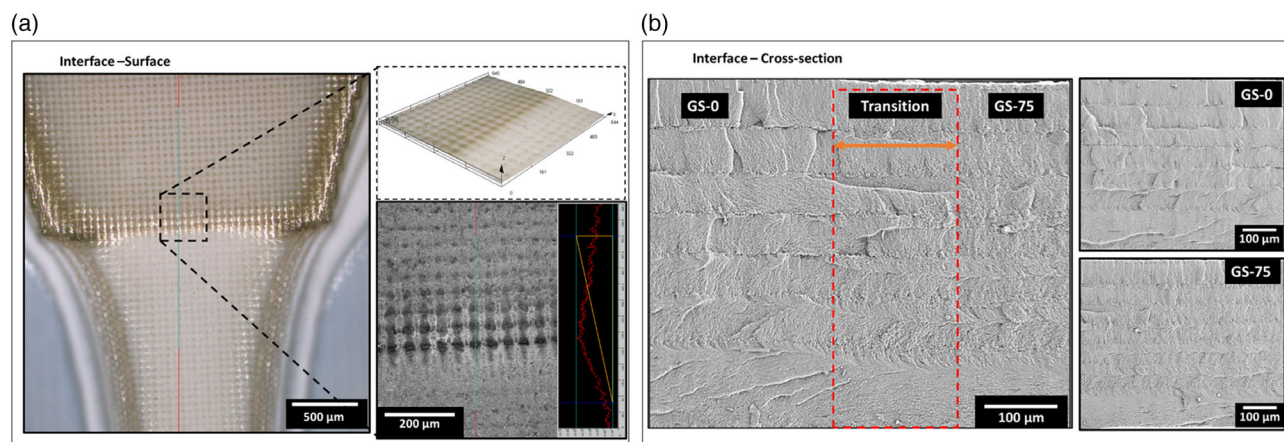


Figure 6. Interface analysis: a): Images recorded using a profilometer representing the surface profile at the interface between GS-0 and GS-75. Morphological transition can be observed with 3–4 pixels wide. The surface profile image represents the dip toward the GS-75 region compared to GS-0, developed due to different shrinkage rates. b): Cross-sectional SEM recorded at the interface between GS-0 and GS-75. A transition from the dense, layered structure (GS-0) to the porous polymer monolith structure (GS-75) can be observed. The interface width equivalent to 3–4 pixels can be observed (left). Cross-sectional images representing the distinctive structural differences at GS-0 and GS-75 besides the interface area (right).

polymerization due to the diffusion of radicals before these are removed by the photoabsorber. Despite this, the SEM images recorded adjacent to the transition zones show the dense, layered structure with a smooth surface finish for GS-0 and granulated, rough, porous structure for GS-75 (Figure 6b (right)).

3.4.2. Membrane-Integrated Device for Soil Analysis

The colorimetric reagent used for the iron assay, a 1:1 mixture of 1,10 phenanthroline and hydroxylamine hydrochloride, was loaded into the reagent reservoir (volume of 20 μL). The calibration standard or soil slurry was added to the second reservoir. The solutes (target analyte and reagents) penetrate the porous barrier, leaving soil particulates behind. Since the iron in the sample was reduced by hydroxylamine, with a conversion of Fe^{3+} to Fe^{2+} , the Fe (II)- 1,10 phenanthroline complexes accounted for the characteristic orange color developed in the porous area, with its intensity indicative of the amount of iron in the sample. The test zone was photographed every minute for over 40 min, and the blank-corrected color intensity was analyzed (Figure S8, Supporting Information). The optimum time (10 min) was defined as the shortest time that allowed for differentiation of the target concentration range in a statistically significant way. A linear calibration curve ($y = 0.559x + 4.427$, $R^2 = 0.992$) was obtained for Fe^{3+} over the range of 25–250 mg L^{-1} ($n = 3$ devices; Figure 7a). The limit of detection (LOD) was determined based on standard methods (19 mg L^{-1}).^[36] The total iron concentration ($\text{Fe}^{3+}/\text{Fe}^{2+}$) in a soil slurry was determined, with the porous barrier enabling clear observation of the colorimetric reaction (Figure 7b). The iron concentration in the soil sample was determined to be $155 \pm 8 \text{ mg L}^{-1}$ ($n = 3$), in excellent agreement ($<2\%$) with the confirmatory analysis conducted by inductively coupled plasma–atomic emission spectrometry (ICP-AES).

The sensitivity of the presented method is lower than that of the method developed on a PIP 3D-printed device (LOD = 1 mg L^{-1}).^[9] However, the presented method covers a more extensive concentration range (19–250 mg L^{-1} vs.

1–15 mg L^{-1}), making it more suitable for the soil samples analyzed (iron $155 \pm 8 \text{ mg L}^{-1}$).

4. Conclusion and Prospects

The 3D printing of hierarchically porous structures within an individual print layer was realized by combining G-DLP with PIPS ink. Using this ink formulation, dense and porous materials were printed with spatial precision, providing access to FGM. The geometrical density of the printed materials ranged from 1.01 g cm^{-3} for GS-75 to 1.21 g cm^{-3} for GS-0, and the porosity ranged from 23% for GS-75 to 0.8% for GS-0. Most pronounced changes in porous properties were found for grayscales ranging from GS-45 to GS-75; at grayscale intensities beyond GS-75, the dose was insufficient for complete polymerization, leading to the printing of incomplete objects. Of significance for fluidic applications, no wicking was observed in the material printed at GS-0, while an aqueous solution progressed 4.4 mm in the first hour through the material printed at GS-75. A functionally integrated fluidic device was printed from a single ink using the grayscale mask to combine wicking and nonwicking materials. The device was used for soil analysis using a colorimetric iron assay, with the quantitative result of 155.81 mg L^{-1} within 2% of the confirmatory chemical analysis. The presented 3D printing method allows for one-step functional integration, eliminating cumbersome multilayer assembly, gluing, and sealing steps required for membrane integration using traditional microfabrication methods. Additionally, porosity control is obtained by modulation of the grayscale intensity, providing access to sought-after functionally graded porous materials.

Future technology advances are in developing specific surface functionalities through the development of advanced ink formulations. Tailoring these materials is anticipated to lead to wide-ranging applications such as sorbent or catalysts, energy storage, and printing biomimetic materials for cell culture and regenerative medicine.

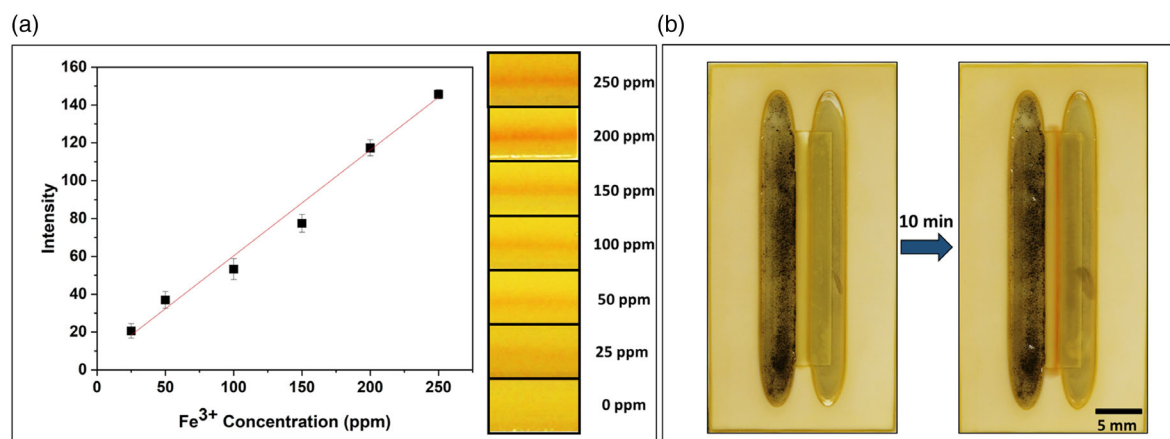


Figure 7. Soil analysis: a) Calibration relating the color intensity with Fe^{3+} concentration for concentrations ranging from 0 to 250 ppm, with error bars reflecting the standard deviation for $n = 3$ devices (left); photographs of color changes in the porous barrier for standard solutions (right). b) The device containing the soil sample in the left reservoir and reagents in the right reservoir (left) shows the color change in the porous barrier after 10 min (right).

5. Experimental Section

Printing Process and Equipment: A commercial DLP 3D printer, Phrozen Shuffle 2018 (Phrozen Tech, Co, Ltd, Taiwan), was used to develop materials (Figure S1a, Supporting Information). The printer worked based on the liquid crystal display (LCD)-DLP 3D printing technique, with an X–Y screen resolution of $47 \times 47 \mu\text{m}$ and build plate dimensions of $120 \times 70 \text{ cm}$. The in-built software interface NanoDLP (Phrozen) had the ability to introduce a grayscale mask into the sliced layers.

Formulation of Inks: For all hybrid ink formulations discussed, poly (ethylene glycol diacrylate), with a molecular weight of 250 Da (PEGDA-250) (Sigma-Aldrich, NSW, Australia), was used as the monomer. In addition, 2,4,6-trimethyl benzoyl phenyl phosphinate (TPO) (Sigma-Aldrich, NSW, Australia) was used as the photoinitiator. Sudan Orange (Sigma-Aldrich, NSW, Australia) was used as the photoabsorber.

The ink was prepared by combining PEGDA-250 and methanol in a ratio of 58% and 42% (v v^{-1}), adding 3% (w w^{-1}) of TPO (29.4 mg mL^{-1}) with 0.015% (w w^{-1}) of Sudan orange (1.65 mg mL^{-1}) to PEGDA-250 and methanol mixture. The nonporogen-containing DLP ink was prepared by mixing 3% (w w^{-1}) of TPO (29.4 mg mL^{-1}) with 0.015% (w w^{-1}) of Sudan orange (1.65 mg mL^{-1}) with PEGDA-250.

Pore Distributions and Porosity Measurements: Sample preparation for scanning electron microscopy (SEM) cross-section imaging for interlayer analysis: samples were broken in half and polished along their cross section using a 1000 grit sandpaper to remove irregularities and achieve a flat cross section, followed by a 4000-grit sandpaper for 5 min. In addition, $3 \mu\text{m}$ diamond paper and $0.25 \mu\text{m}$ diamond paper were used to finish polishing for 5 min each. All polishing steps were conducted while flushing with water and samples were sonicated for 10 min between each step. Samples were air dried and coated with a 10 nm-thick layer of Au/Pd (PECS, Gatan) before being loaded inside the SEM (Quanta 250, FEI, USA). Samples for the SEM-focused ion beam (SEM-FIB) imaging were prepared by three-stage milling processes under 30 keV using 3 nA for raw milling, followed by 0.1 nA for polishing and finishing milling. Images were recorded at an angle of 52° using FIB-SEM (Quanta 3D, FEI, USA). Multigrayscale samples were cross sectioned in liquid nitrogen and coated with Au nanoparticles (thickness 5 nm) using Leica ACE600. Cross sections were imaged in SEM at 4 kV using the in-lens for detecting backscattered electrons (Supra 55VP, Zeiss).

The pore size information from the 2D SEM images was obtained by following the published routines.^[19] First, raw SEM images were corrected for brightness gradients, and a Gaussian median filter was applied to reduce pixel noise. Polymer particles corresponded to light-gray colors and pores to dark colors in this image. Due to the finite penetration depth during imaging, intermediate gray values corresponded to polymer particles that were not in direct contact. Later a threshold was calculated using Otsu's method,^[37] and the image was binarized and overlaid onto the original image. After that, the Euclidean distance transform was determined by calculating the distance to the next white pixel for each pixel and encoding the result as a gray value. By identifying local maxima, circles could then be fitted, and the pore size distribution can be obtained by organizing the fitted circles' obtained diameters as a histogram.

Geometrical density was calculated from mass and volume, measured from 3D-printed samples with 5 mm diameter and 0.5 mm thickness. The geometrical volume of the sample combined the volume of the skeletal structure and the air filling the pores. An ultrapycnometer (Ultrapy 1200e, Quantachrome Instruments, Australia) was used for measuring the skeletal volume/true volume of the sample in the microcells at the ambient temperature (21°C) using helium as the operating gas at 19 psi. The percentage porosity (ϵ) was calculated from the geometrical and true volume. Surface roughness and surface profile data were obtained from the LEXT OLS4100 3D laser microscope (Olympus, Australia). The equipment used laser scanning to perform noncontact 3D measurements of complex surface features. Chemical structure data were obtained from the Bruker Lumos Fourier Transform Infrared Microscope (Bruker, Australia) in the attenuated total reflectance (ATR) mode.

All material characterization tests were conducted after air drying, resulting in shrinkage (5.7–6.4% by volume) after porogen removal. Drying under

supercritical conditions may preserve the porosity of the printed part and prevent shrinkage.^[21] However, this processing requires specialist equipment, making it an unrealistic representation of the material properties obtained using G-DLP for rapid prototyping and manufacturing.

Wicking Tests: The wicking behavior was studied in a 3D-printed device with rectangular pillars (cross-sectional area = $4 \times 0.5 \text{ mm}^2$) connected to a sample reservoir of 20 μL volume capacity. The device was designed with five independent rectangular pillars connected to each reservoir. The computer-aided design (CAD) model was 3D printed using grayscale masks with intensities of GS-0, GS-45, GS-55, GS-65, and GS-75 (where GS-xx represents the percentage grayscale gradient of the mask), respectively, on the pillars. The 3D-printed part follows the standard post-printing treatment (washing and drying). The wicking tests were performed by adding 20 μL of aqueous sample (0.1 M fluorescein dye dissolved in deionized [DI] water) to the sample reservoirs and monitoring the progression of the dye front over the period until the endpoint of the rectangular pillar was reached. The position of the front was monitored by taking timelapse photos every minute for 8 h using a Canon EOS 60D DSLR camera (Canon, Australia). The photographs were analyzed using Image J software (ImageJ)^[38] to determine the wicking characteristics of each pillar with discrete grayscale intensities. The results were plotted using Origin 2020 (Origin Lab, USA). To ensure reproducibility, devices were analyzed in triplicate.

Iron–Phenanthroline Assay: An acetate buffer was prepared with 15.0 g of sodium acetate trihydrate (Sigma-Aldrich, NSW, Australia) and 11.75 mL of glacial acetic acid (Sigma-Aldrich, NSW, Australia) in 50 mL of DI water, resulting in a 6.3 M acetate solution of pH 4.5. Both 1,10-phenanthroline (8 mg L^{-1}) (Sigma-Aldrich, NSW, Australia) and hydroxylamine (0.1 g mL^{-1}) (Sigma-Aldrich, NSW, Australia) were prepared as separate solutions, each in the acetate buffer. Iron (III) chloride hexahydrate (Sigma-Aldrich, NSW, Australia) was used to prepare a standard metal solution (1,000 ppm) by dissolving 1.45 mg mL^{-1} of DI water. Standard Fe^{3+} solutions in the range of 25–250 ppm were prepared from the stock solution by dilution. This range was selected from expected Fe^{3+} concentrations in soil collected from the Wurdiboluc water treatment plant from Barwon Water, Victoria, Australia.

Following the typical process, a 3D-printed device for the soil analysis was designed with two parallel chambers ($30 \times 3 \times 0.5 \text{ mm}$) separated by a porous barrier (width = 2 mm). Grayscale masks with GS-0 and GS-75 were used in the device while 3D printed. This led to a completely dense (non-wicking) structure in the GS-0 region and a porous (wicking) structure in the GS-75 region. The calibration plot was generated using standard solutions of iron chloride hexahydrate. To perform the assay, a mixture of 1,10 phenanthroline and hydroxylamine hydrochloride (1:1) was prepared, 20 μL was deposited in one of the chambers, and the same volume of the Fe^{3+} standard solution was deposited in the other chamber. The solutions diffused only through the porous area, leaving the particulate matter from the soil, to form an orange color ($\text{Fe(II)} \cdot 1,10$ phenanthroline complex). The test zone was photographed using a Canon EOS 60D DSLR camera (Canon, Australia) over 40 min, and blank-corrected color intensity evolution was analyzed using Image J software. The raw images were converted to 8-bit images, and the threshold was adjusted to the required color. The color intensity derived from the 8-bit image was plotted for different concentrations to yield the calibration curve, in line with previously published works.^[34]

Supporting Information

Supporting Information is available from the Wiley Online Library or from the author.

Acknowledgements

H.K.B. acknowledges the receipt of a scholarship from Deakin University's Faculty of Science, Engineering, and Built Environment and the Institute of Frontier Materials. Minh Duc Nguyen (Deakin University) is acknowledged for helping with the soil sample collection and inductively coupled plasma

atomic emission spectrometry analysis. Dr. Sareh Zhand (University of Technology Sydney) is acknowledged for helping with scanning electron microscopy imaging. R.M.G. acknowledges she is investigator on a research grant from the Australian Research Council Linkage Project (LP160101247) with Young Optics, Inc. L.F.D. acknowledges Khalifa University through project RC2-2019-007. D.Y. acknowledges Alfred Deakin Postdoctoral Fellowship from Deakin University.

Conflict of Interest

The authors declare no conflict of interest.

Author Contributions

H.B. took care of formal analysis, investigation, methodology, validation, visualization, and writing the original draft; L.D. looked after conceptualization, formal analysis, funding acquisition, investigation, methodology, project administration, resources, supervision, visualization, and writing the review and editing; A.M. looked after formal analysis, investigation, supervision, visualization, and writing the review and editing. C.A. took care of formal analysis, methodology, and visualization; D.Y. looked after formal analysis, methodology, supervision, visualization, and writing the review and editing; E.D. conducted conceptualization, investigation, methodology, supervision, and writing the review and editing; R.G. took care of conceptualization, funding acquisition, methodology, project administration, resources, supervision, visualization, and writing the review and editing.

Data Availability Statement

The data that support the findings of this study are available from the corresponding author upon reasonable request.

Keywords

3D printing, digital light projections, functionally graded porous structures, grayscale, integrated fluidic devices, membranes

Received: October 24, 2022

Revised: December 16, 2022

Published online: January 17, 2023

- [1] M. Costantini, J. Jaroszewicz, Ł. Kozioł, K. Szlęzak, W. Świąszkowski, P. Garstecki, C. Stubenrauch, A. Barbeta, J. Guzowski, *Angew. Chem., Int. Ed.* **2019**, *58*, 7620.
- [2] J. de Jong, R. G. H. Lammertink, M. Wessling, *Lab Chip* **2006**, *6*, 1125.
- [3] Y. Li, Z. Feng, L. Hao, L. Huang, C. Xin, Y. Wang, E. Bilotti, K. Essa, H. Zhang, Z. Li, F. Yan, T. Peijs, *Adv. Mater. Technol.* **2020**, *5*, 1900981.
- [4] M. J. Dalby, N. Gadegaard, R. O. C. Oreffo, *Nat. Mater.* **2014**, *13*, 558.
- [5] B. Notario, J. Pinto, M. A. Rodriguez-Perez, *Prog. Mater. Sci.* **2016**, *78–79*, 93.
- [6] I. Gibson, D. W. Rosen, B. Stucker, M. Khorasani, *Additive Manufacturing Technologies*, Vol. 17, Springer, New York **2021**.
- [7] Q. Chen, P.-F. Cao, R. C. Advincula, *Adv. Funct. Mater.* **2018**, *28*, 1800631.
- [8] H. K. Balakrishnan, E. H. Doeven, A. Merenda, L. F. Dumée, R. M. Guijt, *Anal. Chim. Acta* **2021**, *1185*, 338796.
- [9] S. Keshan Balavandy, F. Li, N. P. Macdonald, F. Maya, A. T. Townsend, K. Frederick, R. M. Guijt, M. C. Breadmore, *Anal. Chim. Acta* **2021**, *1151*, 238101.
- [10] F. Li, N. P. Macdonald, R. M. Guijt, M. C. Breadmore, *Anal. Chem.* **2019**, *91*, 1758.
- [11] F. Li, P. Smejkal, N. P. Macdonald, R. M. Guijt, M. C. Breadmore, *Anal. Chem.* **2017**, *89*, 4701.
- [12] L. Alison, S. Menasce, F. Bouville, E. Tervoort, I. Mattich, A. Ofner, A. R. Studart, *Sci. Rep.* **2019**, *9*, 409.
- [13] H. Gong, B. P. Bickham, A. T. Woolley, G. P. Nordin, *Lab Chip* **2017**, *17*, 2899.
- [14] D. W. Johnson, C. Sherborne, M. P. Didsbury, C. Pateman, N. R. Cameron, F. Claeysens, *Adv. Mater.* **2013**, *25*, 3178.
- [15] X. Mu, T. Bertron, C. Dunn, H. Qiao, J. Wu, Z. Zhao, C. Saldana, H. J. Qi, *Mater. Horiz.* **2017**, *4*, 442.
- [16] N. Pei, Z. Hao, S. Wang, B. Pan, A. Fang, J. Kang, D. Li, J. He, L. Wang, *Int. J. Bioprint.* **2021**, *7*, 359.
- [17] F. Wang, P. Altschuh, L. Ratke, H. Zhang, M. Selzer, B. Nestler, *Adv. Mater.* **2019**, *31*, 1806733.
- [18] F. Svec, M. J. Fréchet Jean, *Science* **1996**, *273*, 205.
- [19] F. Mayer, D. Ryklin, I. Wacker, R. Curticean, M. Čalkovský, A. Niemeyer, Z. Dong, P. A. Levkin, D. Gerthsen, R. R. Schröder, M. Wegener, *Adv. Mater.* **2020**, *32*, 2002044.
- [20] D. G. Moore, L. Barbera, K. Masania, A. R. Studart, *Nat. Mater.* **2020**, *19*, 212.
- [21] Z. Dong, H. Cui, H. Zhang, F. Wang, X. Zhan, F. Mayer, B. Nestler, M. Wegener, P. A. Levkin, *Nat. Commun.* **2021**, *12*, 247.
- [22] C. Ortiz, M. C. Boyce, *Science* **2008**, *319*, 1053.
- [23] L. Rossetti, L. A. Kuntz, E. Kunold, J. Schöck, K. W. Müller, H. Grabmayr, J. Stolberg-Stolberg, F. Pfeiffer, S. A. Sieber, R. Burgkart, A. R. Bausch, *Nat. Mater.* **2017**, *16*, 664.
- [24] X. Kuang, J. Wu, K. Chen, Z. Zhao, Z. Ding, F. Hu, D. Fang, H. J. Qi, *Sci. Adv.* **2019**, *5*, eaav5790.
- [25] J. Li, M. Pumera, *Chem. Soc. Rev.* **2021**, *50*, 2794.
- [26] H. Gong, M. Beauchamp, S. Perry, A. T. Woolley, G. P. Nordin, *RSC Adv.* **2015**, *5*, 106621.
- [27] S. Yu, F. L. Ng, K. C. C. Ma, F. L. Ng, J. Zhao, S. K. K. Tong, *J. Appl. Polym. Sci.* **2011**, *120*, 3190.
- [28] Y. Li, H. Dennis Tolley, M. L. Lee, *J. Chromatogr., A* **2010**, *1217*, 4934.
- [29] F. Svec, *J. Chromatogr., A* **2010**, *1217*, 902.
- [30] F. Svec, *J. Chromatogr., A* **2012**, *1228*, 250.
- [31] J. A. Deverell, T. Rodemann, J. A. Smith, A. J. Canty, R. M. Guijt, *Sens. Actuators, B* **2011**, *155*, 388.
- [32] V. Shkolnikov, D. G. Strickland, D. P. Fenning, J. G. Santiago, *Sens. Actuators, B* **2010**, *150*, 556.
- [33] C. Achille, C. Parra-Cabrera, R. Dochy, H. Ordutowski, A. Piovesan, P. Piron, L. Van Looy, S. Kushwaha, D. Reynaerts, P. Verboven, B. Nicolaï, J. Lammertyn, D. Spasic, R. Ameloot, *Adv. Mater.* **2021**, *33*, 2008712.
- [34] M. M. Mentale, J. Cunningham, K. Koehler, J. Volckens, C. S. Henry, *Anal. Chem.* **2012**, *84*, 4474.
- [35] T. Müllner, A. Zankel, F. Svec, U. Tallarek, *Mater. Today* **2014**, *17*, 404.
- [36] F. Allegrini, A. C. Olivieri, *Anal. Chem.* **2014**, *86*, 7858.
- [37] N. Otsu, *IEEE Trans. Syst. Man Cybern.* **1979**, *9*, 62.
- [38] C. A. Schneider, W. S. Rasband, K. W. Eliceiri, *Nat. Methods* **2012**, *9*, 671.